



# Multifunctional potassium thiocyanate interlayer for eco-friendly tin perovskite indoor and outdoor photovoltaics

Jun-Jie Cao<sup>a</sup>, Yan-Hui Lou<sup>b,\*</sup>, Wen-Fan Yang<sup>a</sup>, Kai-Li Wang<sup>a</sup>, Zhen-Huang Su<sup>c</sup>, Jing Chen<sup>a</sup>, Chun-Hao Chen<sup>a</sup>, Chong Dong<sup>a</sup>, Xing-Yu Gao<sup>c</sup>, Zhao-Kui Wang<sup>a,\*</sup>

<sup>a</sup> Institute of Functional Nano & Soft Materials (FUNSOM), Jiangsu Key Laboratory for Carbon-Based Functional Materials & Devices, Soochow University, Suzhou 215123, China

<sup>b</sup> College of Physics, Soochow Institute for Energy and Materials Innovations, Soochow University, Suzhou 215006, China

<sup>c</sup> Shanghai Synchrotron Radiation Facility, Shanghai Advanced Research Institute, Shanghai Institute of Applied Physics, Chinese Academy of Sciences, Shanghai 201204, China



## ARTICLE INFO

### Keywords:

Tin perovskites  
Potassium thiocyanate  
Interfacial layer  
Indoor and outdoor photovoltaics

## ABSTRACT

Serious issues such as easy-oxidation of  $\text{Sn}^{2+}$ , fast crystallization rate and high defect density are still existing in tin perovskites to restrain their photovoltaic performance. Herein, a strategy of bottom passivation by potassium thiocyanate (KSCN) has been developed in  $\text{FA}_{0.75}\text{MA}_{0.25}\text{SnBr}_3$ -based perovskite solar cells. KSCN interlayer exhibited multifunctional roles in aligning energy levels, assisting perovskite crystallization and promoting charge transport. The resulting champion device delivered superior power conversion efficiency (PCE) as high as 11.17% under AM 1.5G illumination. It is worth noting that the champion indoor photovoltaics efficiency under 2956 K@1062 lx (334.41  $\mu\text{W}/\text{cm}^2$ ) illumination could approach 17.57%, which is the highest PCE for tin perovskite photovoltaics to our knowledge. The outstanding indoor performance demonstrates the huge application potential of eco-friendly tin perovskites.

## 1. Introduction

There has been tremendous growth in the perovskite solar cells (PSCs) over the last decade, whose certified power conversion efficiency (PCE) has reached 25.5% from 3.8% [1–3]. However, the toxicity of lead in the PSCs has aroused much attention from researchers because of its damages to health and pollution to the environment [4,5]. Tin element seems to be an ideal substitute for lead owing to their similar ionic radius and identical outer electron configuration [6]. In contrast to lead, tin is lower toxic. Especially when it is in the air condition, tin can be degraded into water-insoluble and inactive  $\text{SnO}_2$  which is more eco-friendly [7,8]. In addition, tin perovskite has a tunable bandgap, strong light coefficients and high carrier mobility so that it can be predicted that tin PSCs would be the most extraordinary candidates in the domain of the solar cells [9–11]. Until now, the reported PCEs of tin PSCs have broken 14% accompanied by splendid device stability [12,13].

Nevertheless, there remains a big gap in the performance of tin PSCs compared with that of lead-based counterparts. There are several obstacles to further expedite the development of tin devices, such as the

easy oxidation of  $\text{Sn}^{2+}$ , fast crystallization rate and high defect density coming from the low formation energy of Sn vacancy [14–16]. Especially, few reports are focusing on passivating the defect state from the bottom surface of tin perovskite film to regulate the nucleation, crystallization and growth process of perovskite film, as well as how it can affect their photovoltaic performance. Interfacial engineering is one of the practical solutions where the dangling bonds at the interfaces could be fixed to reduce the defect density and energy level would be aligned to facilitate carrier transfer through the interface [17–20]. Recently, thiocyanate ions ( $\text{SCN}^-$ ) have been reported to order the Pb-I octahedrons and optimize the film morphology, such as  $\text{Pb}(\text{SCN})_2$ , MASCN, urea- $\text{NH}_4\text{SCN}$ , or GuaSCN [21–25]. Because of the similar electron configuration, there is also favorable coordination between tin perovskite and  $\text{SCN}^-$ . The lone electron pairs of S- and N- in the  $\text{SCN}^-$  can be donated to the empty orbital of Sn(II) [26–28]. Gao et al demonstrated multifunctional potassium (KSCN) passivation layer between  $\text{NiO}_x$  and  $\text{MAPbI}_3$  with improved open-circuit voltage and device stability [29]. Thus, the incorporation of  $\text{SCN}^-$  as the modification layer in tin PSCs is expected to fix the dangling bonds, improve the charge transport and suppress the oxidation of tin perovskites.

\* Corresponding authors.

E-mail addresses: [yhlou@suda.edu.cn](mailto:yhlou@suda.edu.cn) (Y.-H. Lou), [zkwang@suda.edu.cn](mailto:zkwang@suda.edu.cn) (Z.-K. Wang).

In this work, we introduced a multifunctional KSCN interlayer between the poly (3,4-ethylenedioxythiophene) polystyrene sulfonate (PEDOT:PSS) layer and the  $\text{FA}_{0.75}\text{MA}_{0.25}\text{SnI}_2\text{Br}$  perovskite layer to fabricate tin PSCs. The KSCN interlayer demonstrated multiple functions, including optimized energy band, improved antioxidation, facilitated perovskite crystallization, multiple ordered crystal orientation, reduced trap density and promoted interfacial carrier transport. The champion PCE of the modified device approached 11.17% under AM 1.5 solar spectrum with the increased shorter-circuit current ( $J_{SC}$ ) from  $14.20 \text{ mA/cm}^2$  to  $20.88 \text{ mA/cm}^2$ . The unencapsulated modified device retained 80% PCE of its summit after 1200 h (50 days), which was tested under the ambient condition and stored in a glovebox without illumination. Finally, we reported the highest indoor efficiency of 17.57% under  $2956 \text{ K}@1062 \text{ lx}$  ( $334.41 \mu\text{W/cm}^2$ ) illumination for KSCN-included tin perovskite solar cells.

## 2. Materials and methods

### 2.1. Materials

KSCN (99.99% metal basis) was purchased from Aladdin. Formamidinium bromide (FABr) and methylammonium bromide (MABr) were purchased from Greatcell Solar Materials Pty Ltd.  $\text{SnI}_2$  (99.999%) were purchased from Libra New Energy Technology company. Bphen (> 99%, HPLC) and ethylenediamine diiodide (EDADI) were purchased from Xi'an Polymer Light Technology Corp. Tin (II) fluoride ( $\text{SnF}_2$ , 99%) was purchased from Aldrich. ICBA was purchased from 1-Material. DMF (99.8%), DMSO (99.8%), isopropyl alcohol (IPA) and Chlorobenzene (CB) were purchased from Sigma Aldrich. PEDOT:PSS (P VP AI 4083) was bought from Heraeus. Toluene was purchased from YONGHUA Chemical Company. All the materials were used as received without further purification. FTO was purchased from Advanced Election Technology Co., Ltd.

### 2.2. Solution Preparations

The  $0.8 \text{ M } \text{FA}_{0.75}\text{MA}_{0.25}\text{SnI}_2\text{Br}$  precursor solution was prepared by the mixture of FABr, MABr,  $\text{SnI}_2$ ,  $\text{SnF}_2$ , EDADI in the molar ratio of 0.75: 0.25: 0.1: 0.1: 0.02, then dissolved in a mixed solvent (DMF: DMSO = 9:1 v/v). Different masses of KSCN were added in DMF with concentrations of 5 mg/ml, 10 mg/ml and 15 mg/ml. ICBA was prepared by 20 mg/ml in CB and Bphen was 0.7 mg/ml in IPA.

### 2.3. Device Fabrication

FTO substrates were cleaned by detergent water, acetone and ethanol twice, then dried in an oven to dry out and treated with UV-ozone for 30 min. PEDOT:PSS was spin-coated on the substrates at 500 rpm for 10 s and 4500 rpm for 50 s in the ambient, followed by 140 °C annealing for 15 min.  $60 \mu\text{L}$  KSCN solution of different concentrations was spin-coated at 3000 rpm for 30 s on the PEDOT:PSS layer. Next, the perovskite precursors were deposited on the substrates with the spin-coating speed of 5000 rpm for 30 s and  $180 \mu\text{L}$  toluene was dropped at the seventh second. The substrate was then annealed at 70 °C for 5 min. Subsequently, ICBA solution and Bephen solution were spin-coated at 2000 rpm for 40 s and 3000 rpm for 50 s, respectively. Finally, Ag with thicknesses of 120 nm was deposited by thermal evaporation under the pressure of  $< 4 \times 10^{-6}$  Torr. The area of the devices is  $0.0725 \text{ cm}^2$ .

### 2.4. Characterizations

XPS and UPS analyses were done by using an ESCALAB250Xi (Thermo Fisher Scientific, USA). Time of Flight-Secondary Ion Mass Spectroscopy (ToF-SIMS) was performed on a TOF.SIMS 5 (ION TOF GmbH Germany, 225332). In-situ GIWAXS test was performed at the BL14B1 beamline of China Shanghai Synchrotron Radiation Facility

(SSRF). The SEM images were collected through a field-emission microscopy (Gemini 500, Carl Zeiss). The XRD patterns were obtained by a PAN analytical 80 equipment (Empyrean, Cu Ka radiation). FTIR was tested by the machine from Germanic Bruck. The steady-state PL spectra were acquired using NIR-visible fluorescence spectrometer (FL3, HORIBA). The time-resolved PL spectra were obtained on transient fluorescence spectrometer (HORIB-FM-2015, France JY). The absorption spectra were obtained using UV-Vis spectrophotometer (PerkinElmer Lambda 750). The current density–voltage ( $J-V$ ) curves of solar cells were measured with a programmable Keithley 2400 source meter under the illumination of AM 1.5G ( $100\text{mW cm}^{-2}$ ). Device stability measurement process: At the first time, we measured the devices about 1 h in ambient conditions; Afterwards, we measured the devices for about 10 min every time; we measured the devices every one or two days in the beginning of 200 h; Then, to reduce the influence of oxygen on the devices, we measured the devices every 5 days. A luxmeter (LX-1330B) with fluorescent lamps (Osram L18W/827) was used to get the indoor  $J-V$  curves under  $2956 \text{ K}@1062 \text{ lx}$  ( $334.41 \mu\text{W/cm}^2$ ) illumination. The CAs of the grid lines were measured by a PSSOCA20 optical contact-measuring system.

## 3. Results and discussion

The schematic device structure of tin PSCs is shown in Fig. 1a with the structure of FTO glass/PEDOT:PSS/ $\text{FA}_{0.75}\text{MA}_{0.25}\text{SnI}_2\text{Br}/\text{Indene-C}_60$  bisadduct (ICBA)/4,7-di (phenyl)-1,10-phenanthroline (Bphen)/Ag. KSCN crystalline powder was dissolved in N, N-dimethylformamide (DMF) and spin-coated on the PEDOT:PSS layer without annealing. Subsequently, the mixed organic and Br-I mixed tin perovskite precursors were deposited whose solvents were dimethyl sulfoxide (DMSO) and DMF. In the process of deposition, potassium and thiocyanate ions would permeate both sides of the interlayers because of their high concentration and dissolubility. Consequently, the properties of the PEDOT:PSS layer and perovskite layer would be ameliorated to some extent.

### 3.1. Interfacial and photophysical properties

The ultraviolet-visible (UV-vis) absorption spectra (Figure S1) of the perovskite with different concentrations of KSCN demonstrates a similar absorption band edge. Despite the bottom modification, the perovskite layer still kept a similar energy gap ( $E_g$ ) about 1.63 eV which is much higher than most of the tin perovskite based on the previous works because of the introduction of Br element in our perovskite precursors [30].

To further study the influence of the KSCN interlayer on the up and bottom layer, ultraviolet photoelectron spectra (UPS) measurement was performed to confirm the energy band structure. Fig. 1b shows the UPS spectra of the perovskite without and with the KSCN interlayer. The Fermi level ( $E_F$ ) of the perovskite without and with KSCN interlayer was calculated as  $-4.62 \text{ eV}$  and  $-4.54 \text{ eV}$ , respectively, according to the equation of  $E_F = E_{\text{cut-off}}$  (cut-off binding energy)  $- 21.22 \text{ eV}$  (the released energy that He irradiates). Correspondingly, the valence band ( $E_{VB}$ ) was  $-5.43 \text{ eV}$  and  $-5.20 \text{ eV}$ , respectively, and the conduction band ( $E_{CB}$ ) was  $-3.80 \text{ eV}$  and  $-3.57 \text{ eV}$ , respectively, based on the equations of  $E_{VB} = E_F - E_{F,\text{edge}}$  (Femi edge) and  $E_{CB} = E_{VB} + E_g$ . Meanwhile,  $E_{\text{cut-off}}$  of PEDOT:PSS without and with KSCN interlayer is estimated as  $16.21 \text{ eV}$  and  $16.11 \text{ eV}$ , respectively (Fig. 1c). According to the previous work, when  $E_{F,\text{edge}} = 0$ , work function ( $W_F$ ) can be calculated following the equation of  $W_F = 21.22 - E_{\text{cut-off}}$  [31]. Therefore, the calculated  $W_F$  of PEDOT:PSS changed from  $5.01 \text{ eV}$  to  $5.11 \text{ eV}$  after the covering of KSCN. From the energy level diagram of the device (Fig. 1d), the deeper work function of the PEDOT:PSS matches better with the upshifted  $E_{VB}$  maximum of the perovskite. As it happens, the shallower  $E_{CB}$  minimum of the perovskite optimizes the original mismatched energy level with the  $E_{CB}$  of ICBA ( $\sim 3.74 \text{ eV}$ ) [32].

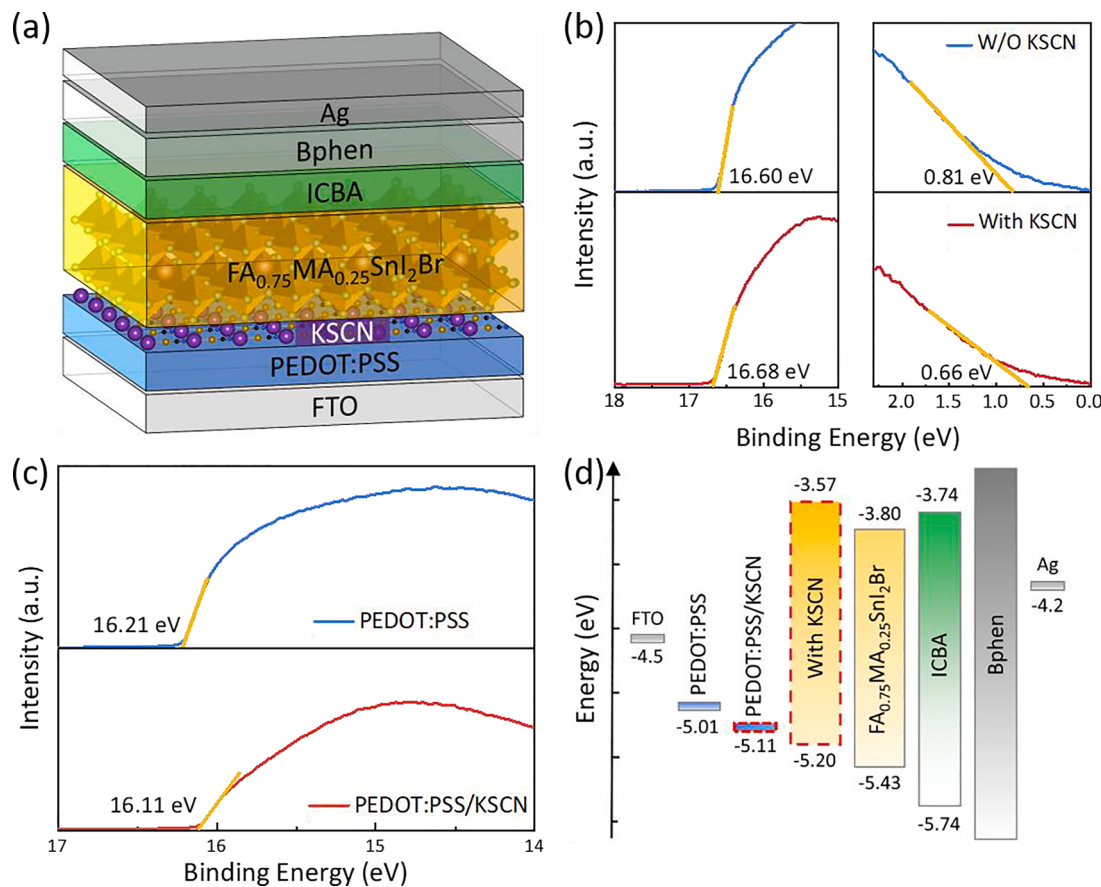


**Fig. 1.** (a) Schematic illustration of the device structure. UPS of (b) perovskite films and (c) PEDOT:PSS films without and with KSCN modification. (d) Energy level diagram of the device.

The X-ray photoelectron spectroscopy (XPS) measurements were conducted to confirm the existence of KSCN on the PEDOT:PSS layer (**Figure S2**). The characteristic peak of K was calibrated to 293 eV for all XPS measurements. XPS measurements of perovskite film with and without KSCN are shown in **Figure S3**. There is no obvious peak of K existing on the surface of perovskite film, suggesting that the potassium ions didn't migrate through the film. Table S1 gives the information of  $\text{Sn}^{2+}$  and  $\text{Sn}^{4+}$  ratios, and corresponding Sn 3d<sub>3/2</sub> XPS patterns are shown in **Fig. 2a to 2b** and **Figure S4**. When the two samples were placed in the identical ambient condition over 1 h, the ratio of  $\text{Sn}^{4+}$  decreased from 44.57% without KSCN to 24.5% with KSCN, which demonstrates that the introduction of  $\text{SCN}^-$  in the interlayers reduced the oxidation of  $\text{Sn}^{2+}$  effectively. The improvement of the antioxidation property of tin PSCs will contribute to the decreased current leakage and enhanced stability of the device [33].

Steady-state and time-resolved photoluminescence (PL) spectra measured at 780 nm for FTO/PEDOT:PSS/perovskite samples with and without KSCN interlayers were conducted to study the influence of KSCN on excited-states in the perovskite films. **Fig. 2c** expresses the steady-state PL where the KSCN modified perovskite film shows the lower PL signal. The enhanced PL quenching effect implicates that the carriers get more efficient when transfer from the perovskite layer to the HTL (**Figure S5**). The slight blue shift of PL indicates the passivation of shallow defects which lay between the maximum of  $E_{VB}$  and the minimum of  $E_{CB}$  [34].

Likewise, time-resolved PL spectra in **Fig. 2d** and **Figure S6**, provide a similar consequence. The biexponential function was used to fit PL lifetime samples which contained a fast decay and slow decay process.  $\tau_1$  is the fast decay denoting the quenching of carries in the perovskite by the way of conveying to the transport layer, and  $\tau_2$  is the slow decay

denoting the radiative decay [35,36]. The data of the time-resolved PL are displayed in Table S2. The decreased  $\tau_1$  from 1.053 ns to 0.559 ns after the modification of the KSCN interlayer indicates its facilitation of the photoinduced free carriers transfer from perovskite to HTL. The decreased lifetime of  $\tau_{avg}$  from 20.889 ns to 3.68 ns further proves the increased diffusion of carriers and efficiency of charge transfer. It could be derived from better energy alignment.

Fourier transform infrared spectroscopy (FTIR) was conducted on the film of PEDOT:PSS, PEDOT:PSS/KSCN and KSCN/SnI<sub>2</sub> (**Figure S7**). The vibrational peak at 2050 cm<sup>-1</sup> is corresponding to the C≡N stretching vibration of SCN<sup>-</sup>, which confirms the existence of KSCN thin film on the surface of PEDOT:PSS [37,38]. There was no existence of an obvious C≡N stretching vibration peak on the KSCN/SnI<sub>2</sub> even with different KSCN concentrations, which indicates the absence of migration to the surface of the perovskite. The result is in accordance with the XPS measurements.

### 3.2. Perovskite crystallization and defects

To preliminarily investigate the influence of KSCN on up and bottom surface, wettability measurements were conducted and demonstrated in **Figure S8**. The water contact angles (CA) of PEDOT:PSS and PEDOT:PSS/KSCN are 21.3° and 31.4°, respectively, which suggests the better hydrophobicity performance. Similarly, when perovskite precursors dropped on the same two films, the CAs were 16.2° and 8.1°, respectively, which indicates that the optimized PEDOT:PSS film yielded superior affinity with the perovskite precursors [39]. The double-function of the modification interlayer may come from the organic solvent of KSCN and the unannealed film.

Top-view scanning electron microscopy (SEM) images in **Fig. 3a to**

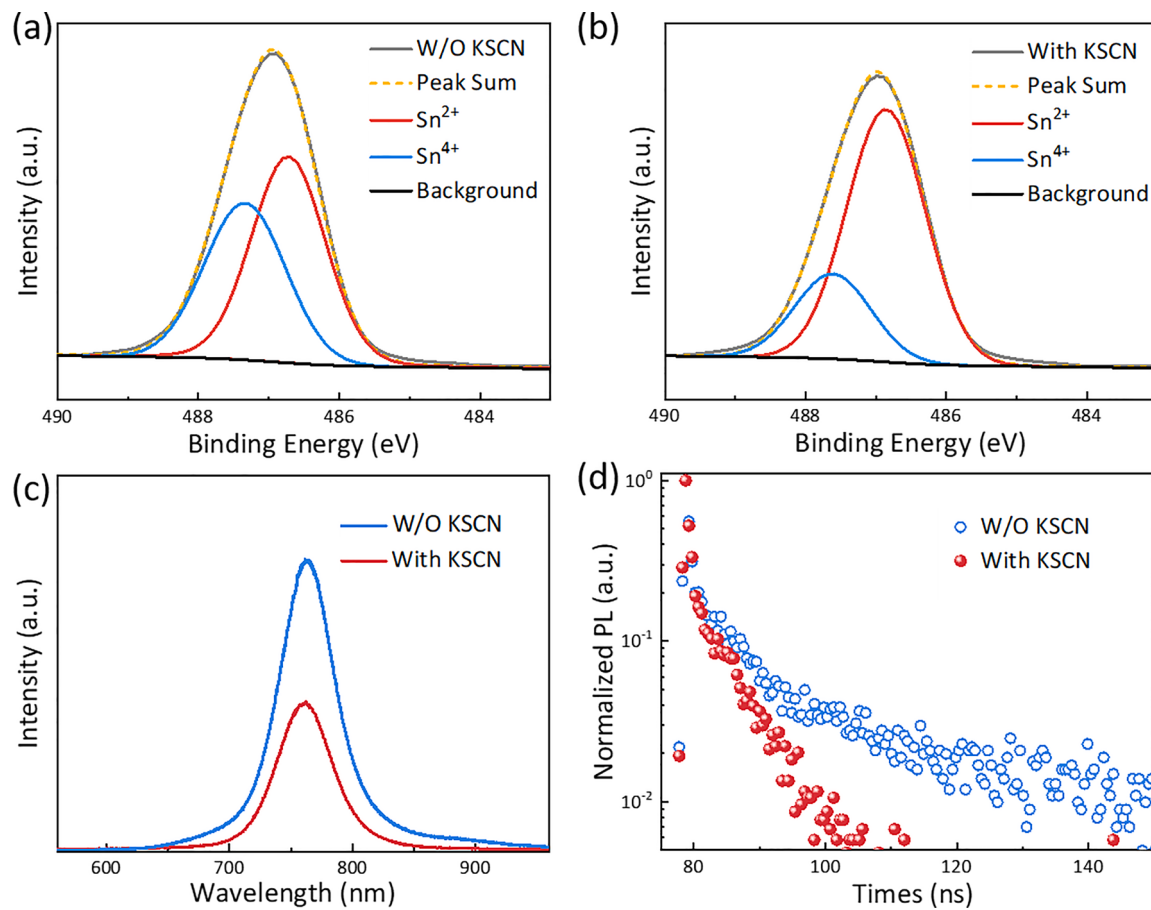


**Fig. 2.** Sn 3d5/2 XPS spectra of (a) pristine perovskite film and (b) KSCN treated perovskite film. (c) Steady-state and (d) PL spectra measured at 780 nm for PEDOT:PSS/perovskite samples with and without KSCN interlayer.

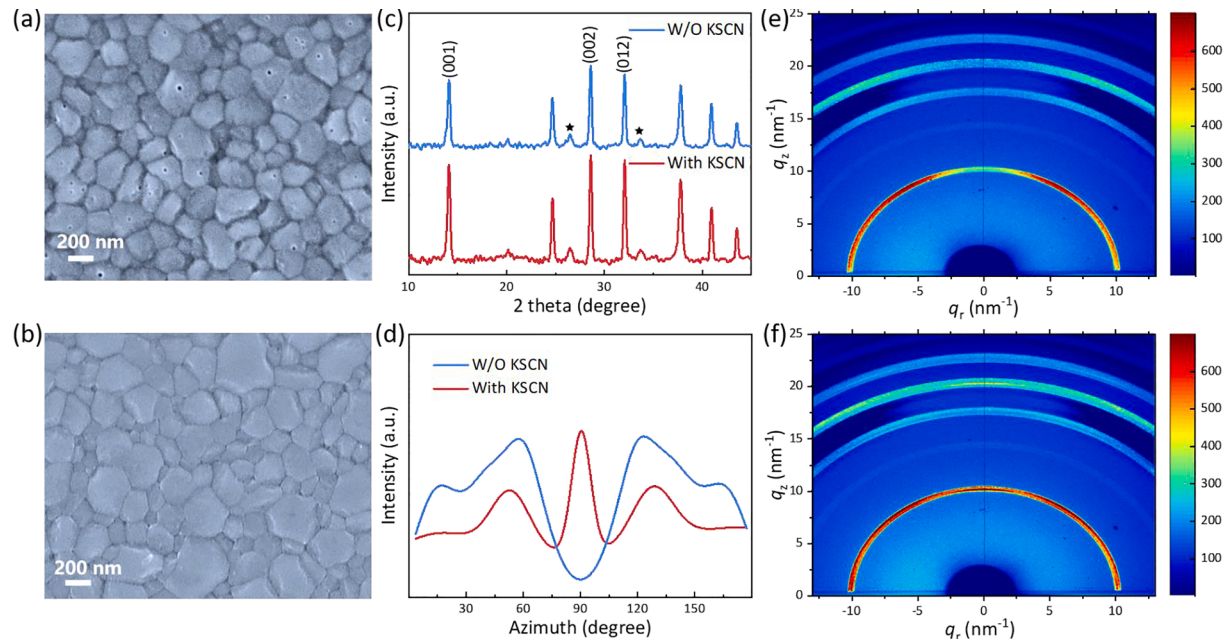


**Fig. 3.** Top-view SEM images of the perovskite films (a) without or (d) with KSCN treatment. (c) XRD pattern of perovskite films without or with KSCN interlayers (★ are on behalf of the peaks of FTO). (d) Radially integrated intensity plots of the GIXRD profiles along the ring at  $q \sim 10.5 \text{ nm}^{-1}$ . GIXRD patterns of perovskite film (e) without or (f) with KSCN treatment.

**3b** show the morphology of perovskite films without and with KSCN interlayers, respectively, which were formed on the FTO/PEDOT:PSS substrate. **Figure S9** reveals the approximate size of the perovskite grains. The optimized perovskite film was almost pin-hole free, suggesting that the introduction of KSCN interlayers may retard the crystal growth rate [40].

**Fig. 3c** shows the X-ray diffraction (XRD) patterns of the perovskite films without and with KSCN interlayer. Dominant peaks at  $14.14^\circ$ ,  $28.60^\circ$ ,  $32.02^\circ$  are assigned to the crystal plane diffraction of (001), (002), (012), respectively. Similar XRD patterns of the perovskite films with different concentrations of KSCN interlayers refer to the unchanged lattice structure of the perovskite. Moreover, the intensity diffraction peaks based on the perovskite films with KSCN modification increased (**Figure S10**), which validated the enhanced crystallinity.

Grazing-incidence X-ray diffraction (GIXRD) measurements (**Fig. 3e** to **3f**) were conducted to probe the crystal orientation of the perovskite films without and with KSCN interlayers. **Fig. 3d** shows the radially integrated intensity plots of the GIXRD profiles along the ring at  $q \sim 10.5 \text{ nm}^{-1}$ . Based on the perovskite film with KSCN modification, there existed an obvious new emerging peak around the azimuth angle of  $90^\circ$  and the intensity of peaks at the azimuth angle around  $55^\circ$  ( $180^\circ - 55^\circ$ ) got weaker. It indicates that the perovskite film with KSCN modification would be beneficial to the formation of multiple ordered crystal orientation and tended to crystallize growing along the vertical direction (out-plane direction) from the pristine slant direction [41,42]. According to previous works, the multiple ordered crystal orientation of the perovskite films and vertical growth of perovskite grains after KSCN modification will facilitate the charge separation and collection [43–45], which is beneficial for the improvement of charge mobilities and  $J_{SC}$  of the perovskite devices. The results will be further confirmed by SCLC and  $J$ - $V$  measurements. What's more, 1D-GXRD spectra as a function of  $q \sim 10.5 \text{ nm}^{-1}$  derived from 2D-GIXRD patterns is displayed in **Figure S11**. The higher diffraction peak based on the perovskite film with KSCN modification indicates better crystallization, which is consistent with the result of XRD measurements [46].

As shown in **Fig. 4a** and **Figure S12**, time-of-flight secondary ions mass spectroscopy (ToF-SIMS) was used to determine the permeation

degree and depth profile of the KSCN interlayer with the structure of FTO/PEDOT:PSS/KSCN/Perovskite/Ag. Here, C≡N and K curve peaks reveal the existence of KSCN interlayer between the HTL and the perovskite layer. It is proved that both potassium and thiocyanate ions extended from the surface of the PEDOT:PSS to the bulk of perovskite. There is no chemical interaction to prohibit  $K^+$  ions from migrating freely. As a result,  $K^+$  ions would exist in the grain boundaries due to their inability to merge into the lattice of perovskite [47,48]. Moreover, they would proceed with bottom-contact passivation and suppress the mutual reaction of halides in the perovskite, which will be proved in the following measurement. In addition, little potassium would infiltrate the surface of the perovskite, which may attribute to its high adsorption energy on the PEDOT:PSS surface. The schematic diagrams of the three-dimensional distribution of bromine ions (in the perovskite layer) and potassium ions (in the KSCN layer) are shown in **Figure S13**, which is in agreement with the result of ToF-SIMS.

The hole-only devices were fabricated with the structure of FTO/PEDOT:PSS (without and with KSCN)/perovskite/P3HT/Au to validate whether the KSCN interlayer influence the trap density ( $N_t$ ) of perovskite films (**Fig. 4b**). The electron-only devices were fabricated with the structure of FTO/TiO<sub>2</sub>(without and with KSCN)/perovskite/ICBA/Ag as shown in **Figure S14**. There are three regions which are the ohmic region, the trap-filled limited region and the space-charge-limited current (SCLC) region [49].  $N_t$  is in the second region and can be calculated by the formula as follows:

$$N_t = 2V_{TFL} \frac{\epsilon_r \epsilon_0}{qL} \quad (1)$$

$L (=150 \text{ nm})$  is the thickness of the tin perovskite layer,  $\epsilon_0 (=8.85 \times 10^{-14} \text{ F/cm})$  is the vacuum permittivity,  $\epsilon_r (=6.5)$  is the relative dielectric constant,  $q (=1.6 \times 10^{-19} \text{ C})$  is the elementary charge and  $V_{TFL}$  is the trap-fill limit voltage which determines the value of  $N_t$ . The  $V_{TFL}$  of the hole-only devices without and with KSCN interlayers were estimated as 1.55 V and 0.53 V, respectively, and the  $N_t$  of the corresponding devices were calculated as  $4.954 \times 10^{16} \text{ cm}^{-3}$  and  $1.694 \times 10^{16} \text{ cm}^{-3}$ , respectively. Similarly, the  $N_t$  of the corresponding electron-only devices could be calculated as  $6.904 \times 10^{16} \text{ cm}^{-3}$  and  $5.625 \times 10^{16} \text{ cm}^{-3}$ , respectively.

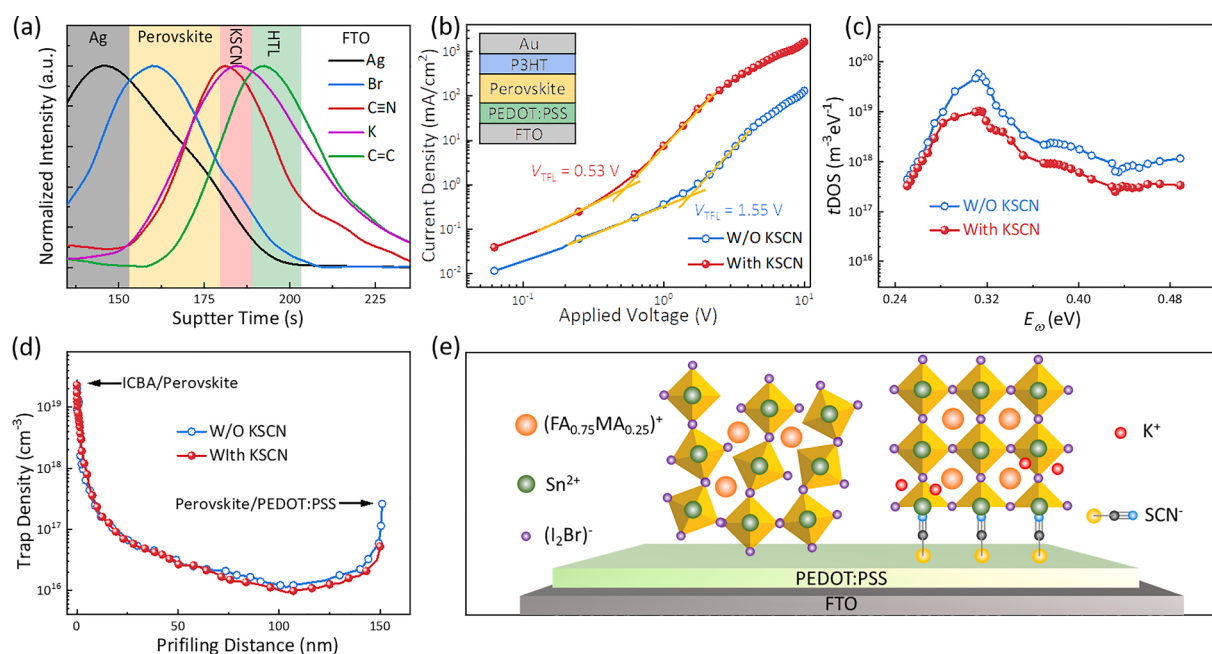


**Fig. 4.** (a) ToF-SIMS depth profiles of the perovskite films deposited on FTO/PEDOT:PSS/KSCN/Perovskite/Ag. (b) Dark I – V curves for the hole-only devices with the structure of FTO/PEDOT:PSS (without and with KSCN)/perovskite/P3HT/Au. (c) tDOS estimation for the devices with or without KSCN modification layer. (d) Dependence of the carrier density on the profiling distance of perovskite films with or without KSCN modified. (e) Schematic crystal orientation of FA0.75MA0.25SnI2Br from (001) without and with KSCN.

As shown in Table S3, the decreased  $N_t$  of both hole-only and electron-only devices verified the effective passivation of KSCN, which will be beneficial to the accelerated charge mobility [50].

At the same time, the charge mobility can be calculated in the SCLC region according to the Mott-Gurney equation:

$$\mu = \frac{8JL^3}{9V^2\varepsilon_r\varepsilon_0} \quad (2)$$

where  $J/V^2$  is the slope of  $J$  versus  $V^2$  in Child's regime [51]. The hole mobilities of the perovskite with and without KSCN interlayers are  $4.48 \times 10^{-3} \text{ cm}^2 \text{ V}^{-1} \text{ s}^{-1}$  and  $2.10 \times 10^{-3} \text{ cm}^2 \text{ V}^{-1} \text{ s}^{-1}$ , respectively. The electron mobilities were increased from  $5.72 \times 10^{-3} \text{ cm}^2 \text{ V}^{-1} \text{ s}^{-1}$  to  $7.64 \times 10^{-3} \text{ cm}^2 \text{ V}^{-1} \text{ s}^{-1}$ . The enhanced charge mobility (Table S3) optimized the charge collection and reduced the recombination.

To further investigate the defect distribution, the trap density of states (tDOS) was performed by thermal admittance spectroscopy (TAS) as shown in Fig. 4c. Deep trap states ( $E_\omega > 0.40 \text{ eV}$ ) come from the surface defects which are resulted from the dangling bonds on the film surface. Shallow trap states ( $E_\omega < 0.35 \text{ eV}$ ) may hail from inside the perovskite [52,53]. The perovskite without KSCN modified displayed 10-fold higher tDOS in the deep trap states than that with modification. It indicates the lower trap density at the interface after the KSCN modification which may reduce the interfacial recombination coming from the surface defects of halide vacancies. Meanwhile, lower trap density in the shallow level certified passivation of the potassium ion migration in the intrinsic of perovskite films. Drive-level capacitance profiling (DLCP) was then used to probe the profiled distribution of the trap density as shown in Fig. 4d. Defects on the profiling distance of  $\sim 150 \text{ nm}$  thick perovskite film implied the reduced trap density at the perovskite/PEDOT:PSS interface which is in agreement with the result of tDOS.

According to the preceding measurements, the proposed schematic crystal structure of the perovskite is depicted in Fig. 4e.  $\text{K}^+$  ions diffused into the perovskite lattice and passivated the defects existing in the grain boundaries.  $\text{SCN}^-$  ions with long electron pairs coordinated with Sn in the tin perovskite, which would restrain the oxidation of Sn(II) and improve the stability of tin PSCs. With the functions of the KSCN interlayer which acted like the lubricant in the PSCs, the energy level got

more suited, leading to the fluent carriers transfer and enhanced charge mobility.

### 3.3. Outdoor and indoor photovoltaic performance

We fabricated the tin perovskite solar devices to further verify the function of the KSCN bottom interlayers. Fig. 5a shows the current-voltage ( $J$ - $V$ ) curves of the pristine device without the KSCN interlayer and the champion device with the KSCN interlayer. The  $J$ - $V$  curves of other devices with different concentrations of KSCN are supplied in Figure S15. The open-circuit voltage ( $V_{OC}$ ) and  $J_{SC}$  improved simultaneously after the KSCN modification and the champion device with 10 mg/ml KSCN shows the highest PCE of 11.17% with a  $V_{OC}$  of 0.82 V,  $J_{SC}$  of  $20.88 \text{ mA/cm}^2$  and fill factor (FF) of 0.64 (Table 1). Compared with the pristine device without modification, there is an obvious improvement of the  $J_{SC}$  and slight amelioration of  $V_{OC}$ . Furthermore, the  $V_{OC}$  is higher than most of the tin PSCs reported. On the one hand, it was attributed to ICBA electron transport layer (ETL), which replaced the generally used PCBM ETL [41]. On the other hand, it came from the introduction of the element bromine (Br) in the X-site which leads to the wider bandgap of the perovskite [54,55]. In addition,

**Table 1**

Parameters of devices with different concentrations of KSCN at AM 1.5G illumination.

KSCN (mg/ml)		$V_{OC}$ (V)	$J_{SC}$ (mA/ $\text{cm}^2$ )	FF	PCE (%)
0	champion	0.78	14.20	0.72	7.89
	average	$0.80 \pm 0.03$	$15.01 \pm 1.08$	$0.71 \pm 0.02$	$7.61 \pm 0.22$
5	champion	0.80	18.21	0.61	8.83
	average	$0.80 \pm 0.01$	$17.58 \pm 0.94$	$0.64 \pm 0.03$	$8.21 \pm 0.55$
10	champion	0.84	20.88	0.64	11.17
	average	$0.82 \pm 0.02$	$20.46 \pm 0.71$	$0.62 \pm 0.03$	$10.54 \pm 0.47$
15	champion	0.83	19.62	0.63	10.23
	average	$0.81 \pm 0.02$	$19.21 \pm 0.54$	$0.61 \pm 0.05$	$9.72 \pm 0.29$

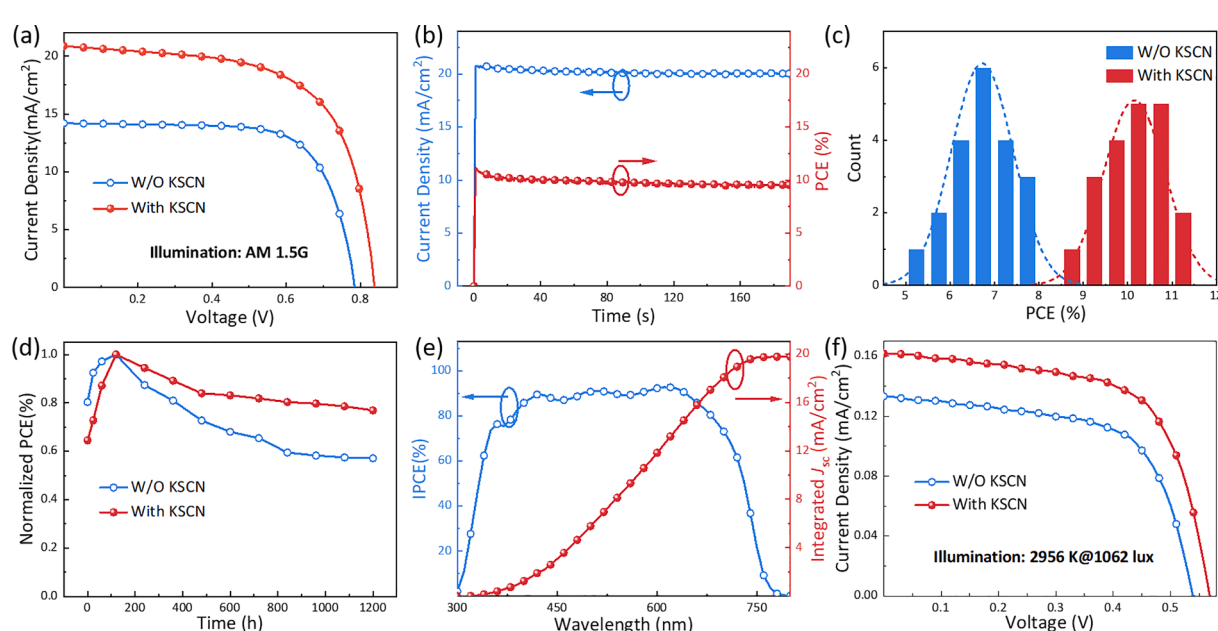


**Fig. 5.** (a)  $J$ - $V$  curves of the devices with or without KSCN treatment under AM 1.5G illumination. (b) Maximum power points of the steady-state current and output PCE for the device with KSCN treatment for 180 s. (c) Histograms of the PCEs for 40 devices with and without KSCN treatment. (d) Normalized PCEs of the unencapsulated devices with or without KSCN treatment. (e) The IPCE spectra and integrated  $J_{SC}$  of the best-performing device. (f) Indoor  $J$ - $V$  curves of the devices with or without KSCN treatment under 2956 K@1062 lux ( $334.41 \mu\text{W}/\text{cm}^2$ ) illumination.

the PCE of 11.17% is one of the highest reported PCEs for mixed-organic and mixed-halogen tin PSCs [56].

Maximum power points of the steady-state current and output PCE for the device with KSCN is provided in Fig. 5b where the photocurrent kept 20.04 mA/cm<sup>2</sup> and the efficiency maintained 9.56%, decreasing by 1.68% after the constant light irradiation about 180 s. The statistics of the PCEs for 40 devices were counted in Fig. 5c to further verify the reproducibility of the pristine and modified devices where the KSCN modified devices identified the superior PCE and reproducibility. Moreover, the stability of the devices without or with KSCN was studied as shown in Fig. 5d. The modified device retained 80% PCE of its summit, whereas the pristine device retained 60% after 1200 h (50 days) due to the favorable anti-oxidation and passivation function of the KSCN interlayer. The unencapsulated devices were tested under ambient condition and stored in a glovebox without illumination. Every time we got the highest efficiency in the process of the stability test, the devices would be put back to the glovebox and there is an obvious rise of PCE in the first 120 h which can be attributed to the self-healing action of the device deriving from the large-volume amines (EDAI<sub>2</sub>) in the perovskite [57].

The incident-photon-to-current efficiency (IPCE) spectra of the perovskite device with 10 mg/ml KSCN interlayers (Fig. 5e) evinces a narrower light response from 300 nm to 780 nm compared with the common FASnI<sub>3</sub> perovskite. It agrees with the absorption spectra of the perovskite film and the integrated  $J_{SC}$  is also in agreement with  $J_{SC}$  from the  $J-V$  curve. The IPCE spectra of the devices with different concentrations of KSCN treatment is shown in Figure S16.

Indoor photovoltaics (IPV) of the perovskite devices have attracted much attention owing to their superior performance and promising application as power sources under the low light circumstance [58–61]. Tin perovskite photovoltaics seem to be a feasible competitor. On the one hand, the relatively higher bandgap (~1.63 eV) of the FA<sub>0.75</sub>MA<sub>0.25</sub>SnI<sub>2</sub>Br perovskite can cover almost all the UV-vis absorption region, as well as partly infrared radiation (IR) region [62]. On the other hand, tin perovskite has a tunable bandgap, strong light coefficients and low exciton binding energy. However, there are still some challenges to further improve the performance of Tin perovskite IPVs. For the reason that the spectral range and intensity of the indoor light sources are far less than those of the sunlight, the typical incident power intensity of indoor light sources is around 300–5000 times smaller than that under the AM 1.5G condition [63]. Hence, the photon-generated carriers from the low light irradiance with a much small number will require a much higher demand on the defects and transport of carriers. Also, the performance of tin perovskite IPVs will be more sensitive to trap density and charge transport [64]. Herein, after the introduction of the KSCN interlayer, there was an obvious decrease in the trap density, which can be proved by the measurements of SCLC and tDOS. In addition, more efficient charge transport was confirmed from the results of PL spectra. These improvements will facilitate the performance of Tin perovskite IPVs.

The perovskite devices were measured under an LED light with the power intensity of 2956 K@1062 lx (334.41 μW/cm<sup>2</sup>) (Table S4) and the emission spectra is shown in Figure S17. Finally, the  $J-V$  curves of the best-performed devices are shown in Fig. 5f and Table 2 to illustrate the feasibility of the IPV application for tin PSCs. It is the highest indoor efficiency of tin PSCs among the reported where the modified device got a champion PCE of 17.57% in comparison with the pristine of 13.57% [65]. Figure S18 shows the PCE distribution histogram of devices with and without KSCN treatment under 1062 lx (334.41 μW/cm<sup>2</sup>) illumination, which was obtained from 30 individual cells.

#### 4. Conclusion

In summary, with the introduction of KSCN interlayers as multi-functional surface modification, FA<sub>0.75</sub>MA<sub>0.25</sub>SnI<sub>2</sub>Br perovskite photovoltaics demonstrated superior outdoor and indoor performance. The

**Table 2**

Parameters of devices with different concentrations of KSCN at 2956 K@1062 lx (334.41 μW/cm<sup>2</sup>) light illumination.

KSCN (mg/ ml)		$V_{OC}$ (V)	$J_{SC}$ (mA/ cm <sup>2</sup> )	FF	PCE (%)	$P_{in}$ (μW/ cm <sup>2</sup> )	$P_{out}$ (μW/ cm <sup>2</sup> )
0	champion	0.54	0.133	0.63	13.57	45.39	334.41
	average	0.53	0.134	0.62	13.12	43.87	
		±	±	±	± 0.32	± 1.07	
10	champion	0.57	0.162	0.64	17.57	58.75	
	average	0.55	0.154	0.64	16.81	56.21	
		±	± 0.05	±	± 0.42	± 1.40	
			0.01		0.01		

interlayer could align the energy level and promote interfacial charge transport. K<sup>+</sup> ions were favorable for the lower trap density while SCN<sup>-</sup> was responsible for improved antioxidation and device stability. Based on the enhanced physical properties and facilitated perovskite crystallization, the champion efficiency of the modified photovoltaics device reached 11.17% compared with pristine 7.89% under AM 1.5G solar irradiation as well as the highest indoor efficiency reported under 2956 K@1062 lx (334.41 μW/cm<sup>2</sup>) illumination of 17.57% in comparison with pristine of 13.57%. The unencapsulated modified device retained 80% PCE of its summit after 1200 h (50 days), which was tested under the ambient condition and stored in a glovebox without illumination. The finding provides a simple and effective method through the modification layer of an inorganic salt to fabricate high-performance tin perovskite photovoltaics. Especially, the outstanding IPV supplies a bright potential of eco-friendly Sn perovskites in future applications.

#### Declaration of Competing Interest

The authors declare that they have no known competing financial interests or personal relationships that could have appeared to influence the work reported in this paper.

#### Acknowledgements

The authors acknowledge financial support from the National Natural Science Foundation of China (Nos. 62075148, 52073197), and the Natural Science Foundation of Jiangsu Province (Nos. BK20201413, BK20211314). This work is supported by Suzhou Key Laboratory of Functional Nano & Soft Materials, Collaborative Innovation Center of Suzhou Nano Science & Technology, the 111 Project, Joint International Research Laboratory of Carbon-Based Functional Materials and Devices, and Soochow University Tang Scholar. The authors thank beamline BL14B1 at the Shanghai Synchrotron Radiation Facility (SSRF) for providing the beam time.

#### Appendix A. Supplementary data

Supplementary data to this article can be found online at <https://doi.org/10.1016/j.cej.2021.133832>.

#### References

- [1] A. Kojima, K. Teshima, Y. Shirai, T. Miyasaka, Organometal halide perovskites as visible-light sensitizers for photovoltaic cells, *J. Am. Chem. Soc.* 131 (17) (2009) 6050–6051, <https://doi.org/10.1021/ja809598r>.
- [2] N.J. Jeon, J.H. Noh, Y.C. Kim, W.S. Yang, S. Ryu, S.I. Seok, Solvent engineering for high-performance inorganic-organic hybrid perovskite solar cells, *Nat. Mater.* 13 (9) (2014) 897–903, <https://doi.org/10.1038/nmat4014>.
- [3] Best research-cell efficiency chart. <https://www.nrel.gov/pv/cell-efficiency.html> (Accessed September 2021).
- [4] A. Abate, Perovskite solar cells go lead free, *Joule* 1 (4) (2017) 659–664, <https://doi.org/10.1016/j.joule.2017.09.007>.

- [5] A. Babayigit, A. Ethirajan, M. Muller, B. Conings, Toxicity of organometal halide perovskite solar cells, *Nat. Mater.* 15 (3) (2016) 247–251, <https://doi.org/10.1038/nmat4572>.
- [6] S. Gu, R. Lin, Q. Han, Y. Gao, H. Tan, J. Zhu, Tin and mixed lead-tin halide perovskite solar cells: progress and their application in tandem solar cells, *Adv. Mater.* 32 (2020) 1907392, <https://doi.org/10.1002/adma.201907392>.
- [7] M. Li, W. Zuo, Y.-G. Yang, M.H. Aldamasy, Q. Wang, S.H.T. Cruz, S.-L. Feng, M. Saliba, Z.-K. Wang, A. Abate, Tin halide perovskite films made of highly oriented 2D crystals enable more efficient and stable lead-free perovskite solar cells, *ACS Energy Lett.* 5 (6) (2020) 1923–1929, <https://doi.org/10.1021/acsenergylett.0c00782.s001>.
- [8] R. Wang, J. Xue, K.-L. Wang, Z.-K. Wang, Y. Luo, D. Fenning, G. Xu, S. Nuryevya, T. Huang, Y. Zhao, J.L. Yang, J. Zhu, M. Wang, S. Tan, I. Yavuz, K.N. Houk, Y. Yang, Constructive molecular configurations for surface-defect passivation of perovskite photovoltaics, *Science* 366 (6472) (2019) 1509–1513.
- [9] L. Xu, X. Feng, W. Jia, W. Lv, A. Mei, Y. Zhou, Q. Zhang, R.-F. Chen, W. Huang, Recent advances in inverted lead-free tin-based perovskite solar cells and challenges, *Energy Environ. Sci.* 14 (2021) 4292–4317, <https://doi.org/10.1039/D1EE00890K>.
- [10] Z. Shi, J. Guo, Y. Chen, Q.i. Li, Y. Pan, H. Zhang, Y. Xia, W. Huang, Lead-free organic-inorganic hybrid perovskites for photovoltaic applications: recent advances and perspectives, *Adv. Mater.* 29 (16) (2017) 1605005, <https://doi.org/10.1002/adma.201605005>.
- [11] C.C. Stoumpos, C.D. Malliakas, M.G. Kanatzidis, Semiconducting tin and lead iodide perovskites with organic cations: phase transitions, high mobilities, and near-infrared photoluminescent properties, *Inorg. Chem.* 52 (15) (2013) 9019–9038, <https://doi.org/10.1021/ic401215x>.
- [12] B.-B. Yu, Z. Chen, Y. Zhu, Y. Wang, B. Han, G. Chen, X. Zhang, Z. Du, Z. He, Heterogeneous 2D/3D tin-halides perovskite solar cells with certified conversion efficiency breaking 14%, *Adv. Mater.* 33 (36) (2021) 2102055, <https://doi.org/10.1002/adma.v33.3610.1002/adma.202102055>.
- [13] X. Jiang, H. Li, Q. Zhou, Q.i. Wei, M. Wei, L. Jiang, Z. Wang, Z. Peng, F. Wang, Z. Zang, K. Xu, Y.i. Hou, S. Teale, W. Zhou, R. Si, X. Gao, E.H. Sargent, Z. Ning, One-step synthesis of SnI<sub>2</sub>(DMSO) adducts for high-performance tin perovskite solar cells, *J. Am. Chem. Soc.* 143 (29) (2021) 10970–10976, <https://doi.org/10.1021/jacs.1c0303210.1021/jacs.1c03032.s001>.
- [14] W. Liao, D. Zhao, Y. Yu, C.R. Grice, C. Wang, A.J. Cimaroli, P. Schulz, W. Meng, K. Zhu, R.-G. Xiong, Y. Yan, Lead-free inverted planar formamidinium tin triiodide perovskite solar cells achieving power conversion efficiencies up to 6.22%, *Adv. Mater.* 28 (42) (2016) 9333–9340, <https://doi.org/10.1002/adma.201602992>.
- [15] S. Shao, J. Liu, G. Portale, H.-H. Fang, G.R. Blake, G.H. ten Brink, L.J.A. Koster, M. A. Loi, Highly reproducible Sn-based hybrid perovskite solar cells with 9% efficiency, *Adv. Energy Mater.* 8 (4) (2018) 1702019, <https://doi.org/10.1002/aenm.201702019>.
- [16] M.H. Kumar, S. Dharani, W.L. Leong, P.P. Boix, R.R. Prabhakar, T. Baikie, C. Shi, H. Ding, R. Ramesh, M. Asta, M. Graetzel, S.G. Mhaisalkar, N. Mathews, Lead-free halide perovskite solar cells with high photocurrents realized through vacancy modulation, *Adv. Mater.* 26 (41) (2014) 7122–7127, <https://doi.org/10.1002/adma.201401991>.
- [17] W. Ke, C. Xiao, C. Wang, B. Saparov, H.-S. Duan, D. Zhao, Z. Xiao, P. Schulz, S. P. Harvey, W. Liao, W. Meng, Y. Yu, A.J. Cimaroli, C.-S. Jiang, K. Zhu, M. Al-Jassim, G. Fang, D.B. Mitzi, Y. Yan, Employing lead thiocyanate additive to reduce the hysteresis and boost the fill factor of planar perovskite solar cells, *Adv. Mater.* 28 (26) (2016) 5214–5221, <https://doi.org/10.1002/adma.201600594>.
- [18] M. Jiang, J. Yuan, G. Cao, J. Tian, In-situ fabrication of P3HT passivating layer with hole extraction ability for enhanced performance of perovskite solar cell, *Chem. Eng. J.* 402 (2020) 126152, <https://doi.org/10.1016/j.cej.2020.126152>.
- [19] M. Li, X. Yan, Z. Kang, Y. Huan, Y. Li, R. Zhang, Y. Zhang, Hydrophobic polystyrene passivation layer for simultaneously improved efficiency and stability in perovskite solar cells, *ACS Appl. Mater. Interfaces* 10 (22) (2018) 18787–18795, <https://doi.org/10.1021/acsm.8b04776.1021/acsm.8b04776.s001>.
- [20] H. Wang, J. Yuan, J. Xi, J. Du, J. Tian, Multiple-function surface engineering of SnO<sub>2</sub> nanoparticles to achieve efficient perovskite solar cells, *J. Phys. Chem. Lett.* 12 (37) (2021) 9142–9148, [https://doi.org/10.1021/acs.jpclett.1c02682.s001](https://doi.org/10.1021/acs.jpclett.1c0268210.1021/acs.jpclett.1c02682.s001).
- [21] H. Lu, Y. Liu, P. Ahlawat, A. Mishra, W.R. Tress, F.T. Eickemeyer, Y. Yang, F. Fu, Z. Wang, C.E. Avalos, B.I. Carlsen, A. Agarwalla, X. Zhang, X. Li, Y. Zhan, S. M. Zakeeruddin, L. EMSLEY, U. Rothlisberger, L. Zheng, A. Hagfeldt, M. Grätzel, Vapor-assisted deposition of highly efficient, stable black-phase FAPbI<sub>3</sub> perovskite solar cells, *Science* 370 (2020) eabb8985, <https://doi.org/10.1126/science.abb8985>.
- [22] B. Yu, J. Shi, S. Tan, Y. Cui, W. Zhao, H. Wu, Y. Luo, D. Li, Q. Meng, Efficient (>20%) and stable all-inorganic cesium lead triiodide solar cell enabled by thiocyanate molten salts, *Angew. Chem. Int. Ed.* 60 (2021) 13436–13443, <https://doi.org/10.1002/anie.202102466>.
- [23] J. Tong, Z. Song, D.H. Kim, X. Chen, C. Chen, A.F. Palmstrom, P.F. Ndione, M. O. Reese, S.P. Dunfield, O.G. Reid, Carrier lifetimes of > 1 μs in Sn-Pb perovskites enable efficient all-perovskite tandem solar cells, *Science* 364 (2019) 475–479, <https://doi.org/10.1126/science.aav7911>.
- [24] H. Kim, Y.H. Lee, T. Lyu, J.H. Yoo, T. Park, J.H. Oh, Boosting the performance and stability of quasi-two-dimensional tin-based perovskite solar cells using the formamidinium thiocyanate additive, *J. Mater. Chem. A* 6 (37) (2018) 18173–18182.
- [25] A. Wijesekara, S. Varagnolo, G.D.M.R. Dabera, K.P. Marshall, H.J. Pereira, R. A. Hatton, Assessing the suitability of copper thiocyanate as a hole-transport layer in inverted CsSnI<sub>3</sub> perovskite photovoltaics, *Sci Rep* 8 (2018) 15722, <https://doi.org/10.1038/s41598-018-33987-7>.
- [26] T. Zöller, L. Iovkova-Berends, T. Berends, C. Dietz, G. Bradtmöller, K. Jurkschat, Intramolecular N–Sn coordination in tin (II) and tin (IV) compounds based on enantiopure ephedrine derivatives, *Inorg. Chem.* 50 (17) (2011) 8645–8653, <https://doi.org/10.1021/ic201203u>.
- [27] C. Gurnani, A.L. Hector, E. Jager, W. Levason, D. Pugh, G. Reid, Tin (II) fluoride vs. tin (II) chloride—a comparison of their coordination chemistry with neutral ligands, *Dalton Trans.* 42 (2013) 8364–8374, <https://doi.org/10.1039/C3DT50743B>.
- [28] D. Sabba, H.K. Mulmudi, R.R. Prabhakar, T. Krishnamoorthy, T. Baikie, P.P. Boix, S. Mhaisalkar, N. Mathews, Impact of anionic Br-substitution on open circuit voltage in lead free perovskite (CsSnI<sub>3</sub>-xBr<sub>x</sub>) solar cells, *J. Phys. Chem. C* 119 (4) (2015) 1763–1767, <https://doi.org/10.1021/jp5126624>.
- [29] Z.-W. Gao, Y. Wang, D. Ouyang, H. Liu, Z. Huang, J. Kim, W.C.H. Choy, Triple interface passivation strategy-enabled efficient and stable inverted perovskite solar cells, *Small Methods* 4 (12) (2020) 2000478, <https://doi.org/10.1002/smtd.v4.1210.1002/smtd.202000478>.
- [30] C. Ferrara, M. Patrini, A. Pisani, P. Quadrelli, C. Milanese, C. Tealdi, L. Malavasi, Wide band-gap tuning in Sn-based hybrid perovskites through cation replacement: the FA 1-x MA x SnBr<sub>3</sub> mixed system, *J. Mater. Chem. A* 5 (19) (2017) 9391–9395, <https://doi.org/10.1039/C7TA01668A>.
- [31] J.H. Jeon, D.H. Wang, H. Park, J.H. Park, O.O. Park, Stamping transfer of a quantum dot interlayer for organic photovoltaic cells, *Langmuir* 28 (25) (2012) 9893–9898, <https://doi.org/10.1021/la301477e>.
- [32] Y. He, H.-Y. Chen, J. Hou, Y. Li, Indene-C<sub>60</sub> bisadduct: a new acceptor for high-performance polymer solar cells, *J. Am. Chem. Soc.* 132 (4) (2010) 1377–1382, <https://doi.org/10.1021/ja908602j>.
- [33] Y. Liao, H. Liu, W. Zhou, D. Yang, Y. Shang, Z. Shi, B. Li, X. Jiang, L. Zhang, L. N. Quan, R. Quintero-Bermudez, B.R. Sutherland, Q. Mi, E.H. Sargent, Z. Ning, Highly oriented low-dimensional tin halide perovskites with enhanced stability and photovoltaic performance, *J. Am. Chem. Soc.* 139 (19) (2017) 6693–6699, <https://doi.org/10.1021/jacs.7b01815.1021/jacs.7b01815.s001>.
- [34] S. Wu, J. Zhang, Z. Li, D. Liu, M. Qin, S.H. Cheung, X. Lu, D. Lei, S.K. So, Z. Zhu, A.-Y. Jen, Modulation of defects and interfaces through alkylammonium interlayer for efficient inverted perovskite solar cells, *Joule* 4 (6) (2020) 1248–1262, <https://doi.org/10.1016/j.joule.2020.04.001>.
- [35] P.-W. Liang, C.-Y. Liao, C.-C. Chueh, F. Zuo, S.T. Williams, X.-K. Xin, J. Lin, A.-Y. Jen, Additive enhanced crystallization of solution-processed perovskite for highly efficient planar-heterojunction solar cells, *Adv. Mater.* 26 (22) (2014) 3748–3754, <https://doi.org/10.1002/adma.201400231>.
- [36] T. Zhao, C.-C. Chueh, Q.i. Chen, A. Rajagopal, A.-Y. Jen, Defect passivation of organic-inorganic hybrid perovskites by diammmonium iodide toward high-performance photovoltaic devices, *ACS Energy Lett.* 1 (4) (2016) 757–763, <https://doi.org/10.1021/acsenergylett.6b00327.1021/acsenergylett.6b00327.s001>.
- [37] L.H. Jones, Infrared spectrum and structure of the thiocyanate ion, *J. Chem. Phys.* 25 (5) (1956) 1069–1072, <https://doi.org/10.1063/1.1743101>.
- [38] L.H. Jones, Polarized infrared spectrum of potassium thiocyanate, *J. Chem. Phys.* 28 (6) (1958) 1234–1236, <https://doi.org/10.1063/1.1744375>.
- [39] J.-J. Cao, K.-L. Wang, C. Dong, X.-M. Li, W.-F. Yang, Z.-K. Wang, Bottom-contact passivation for high-performance perovskite solar cells using TaCl<sub>5</sub>-doped SnO<sub>2</sub> as electron-transporting layer, *Org. Electron.* 88 (2021) 105972, <https://doi.org/10.1016/j.orgel.2020.105972>.
- [40] E. Jokar, C.-H. Chien, A. Fathie, M. Rameez, Y.-H. Chang, E.-G. Diau, Slow surface passivation and crystal relaxation with additives to improve device performance and durability for tin-based perovskite solar cells, *Energy Environ. Sci.* 11 (9) (2018) 2353–2362.
- [41] X. Jiang, F. Wang, Q. Wei, H. Li, Y. Shang, W. Zhou, C. Wang, P. Cheng, Q. Chen, L. Chen, Z. Ning, Ultra-high open-circuit voltage of tin perovskite solar cells via an electron transporting layer design, *Nat. Commun.* 11 (2020) 1245, <https://doi.org/10.1038/s41467-020-15078-2>.
- [42] C.-C. Zhang, S. Yuan, Y.-H. Lou, Q.-W. Liu, M. Li, H. Okada, Z.-K. Wang, Perovskite films with reduced interfacial strains via a molecular-level flexible interlayer for photovoltaic application, *Adv. Mater.* 32 (38) (2020) 2001479, <https://doi.org/10.1002/adma.v32.3810.1002/adma.202001479>.
- [43] W. Hui, L. Chao, H. Lu, F. Xia, Q.i. Wei, Z. Su, T. Niu, L. Tao, B. Du, D. Li, Y. Wang, H.E. Dong, S. Zuo, B. Li, W. Shi, X. Ran, P. Li, H. Zhang, Z. Wu, C. Ran, L. Song, G. Xing, X. Gao, J. Zhang, Y. Xia, Y. Chen, W. Huang, Stabilizing black-phase formamidinium perovskite formation at room temperature and high humidity, *Science* 371 (6536) (2021) 1359–1364.
- [44] Z.-K. Wang, M. Li, Y.-G. Yang, Y. Hu, H. Ma, X.-Y. Gao, L.-S. Liao, High efficiency Pb-In binary metal perovskite solar cells, *Adv. Mater.* 28 (31) (2016) 6695–6703, <https://doi.org/10.1002/adma.201600626>.
- [45] C.-H. Chen, Y.-H. Lou, K.-L. Wang, Z.-H. Su, C. Dong, J. Chen, Y.-R. Shi, X.-Y. Gao, Z.-K. Wang, Ternary two-step sequential deposition induced perovskite orientational crystallization for high-performance photovoltaic devices, *Adv. Energy Mater.* 11 (30) (2021) 2101538, <https://doi.org/10.1002/aenm.202101538>.
- [46] Y. Yang, S. Feng, M. Li, F. Li, C. Zhang, Y. Han, L. Li, J. Yuan, L. Cao, Z. Wang, Enormously improved CH<sub>3</sub>NH<sub>3</sub>PbI<sub>3</sub> film surface for environmentally stable planar perovskite solar cells with PCE exceeding 19.9%, *Nano Energy* 48 (2018) 10–19, <https://doi.org/10.1016/acsenergylett.6b00327>.
- [47] M. Abdi-Jalebi, Z. Andaj-Garmaroudi, S. Cacovich, C. Stavrakas, B. Philippe, J. Richter, M. Alsari, E.P. Booker, E.M. Hutter, A.J. Pearson, S. Lilliu, T.J. Savenije, H. Rensmo, G. Divitini, C. Ducati, R.H. Friend, S.D. Stranks, Maximizing and stabilizing luminescence from halide perovskites with potassium passivation, *Nature* 555 (7697) (2018) 497–501, <https://doi.org/10.1038/nature25989>.

- [48] P. Zhu, S. Gu, X. Luo, Y. Gao, S. Li, J. Zhu, H. Tan, Simultaneous contact and grain-boundary passivation in planar perovskite solar cells using SnO<sub>2</sub>-KCl composite electron transport layer, *Adv. Energy Mater.* 10 (3) (2020) 1903083, <https://doi.org/10.1002/aenm.v10.310.1002/aenm.201903083>.
- [49] J. Chen, X. Zhao, S.-G. Kim, N.-G. Park, Multifunctional chemical linker imidazoleacetic acid hydrochloride for 21% efficient and stable planar perovskite solar cells, *Adv. Mater.* 31 (39) (2019) 1902902, <https://doi.org/10.1002/adma.v31.3910.1002/adma.201902902>.
- [50] J. Xue, R. Wang, X. Chen, C. Yao, X. Jin, K.-L. Wang, W. Huang, T. Huang, Y. Zhao, Y. Zhai, D. Meng, S. Tan, R. Liu, Z.-K. Wang, C. Zhu, K. Zhu, M.C. Beard, Y. Yan, Y. Yang, Reconfiguring the band-edge states of photovoltaic perovskites by conjugated organic cations, *Science* 371 (6529) (2021) 636–640.
- [51] J. Huang, Y. Yuan, Y. Shao, Y. Yan, Understanding the physical properties of hybrid perovskites for photovoltaic applications, *Nat. Rev. Mater.* 2 (2017) 1–19, <https://doi.org/10.1038/natrevmats.2017.42>.
- [52] Y. Shao, Z. Xiao, C. Bi, Y. Yuan, J. Huang, Origin and elimination of photocurrent hysteresis by fullerene passivation in CH<sub>3</sub>NH<sub>3</sub>PbI<sub>3</sub> planar heterojunction solar cells, *Nat. Commun.* 5 (2014) 1–7, <https://doi.org/10.1038/ncomms6784>.
- [53] Z. Ni, C. Bao, Y.e. Liu, Q.i. Jiang, W.-Q. Wu, S. Chen, X. Dai, B.o. Chen, B. Hartweg, Z. Yu, Z. Holman, J. Huang, Resolving spatial and energetic distributions of trap states in metal halide perovskite solar cells, *Science* 367 (6484) (2020) 1352–1358.
- [54] J. Cao, F. Yan, Recent progress in tin-based perovskite solar cells, *Energy Environ. Sci.* 14 (3) (2021) 1286–1325.
- [55] X. Jiang, Z. Zang, Y. Zhou, H. Li, Q.i. Wei, Z. Ning, Tin halide perovskite solar cells: an emerging thin-film photovoltaic technology, *Acc. Mater. Res.* 2 (4) (2021) 210–219, <https://doi.org/10.1021/accountsmr.0c00111>.
- [56] T. Nakamura, S. Yakumaru, M.A. Truong, K. Kim, J. Liu, S. Hu, K. Otsuka, R. Hashimoto, R. Murdey, T. Sasamori, H.D. Kim, H. Ohkita, T. Handa, Y. Kanemitsu, A. Wakamiya, Sn (IV)-free tin perovskite films realized by in situ Sn (0) nanoparticle treatment of the precursor solution, *Nat. Commun.* 11 (1) (2020), <https://doi.org/10.1038/s41467-020-16726-3>.
- [57] C. Ran, W. Gao, J. Li, J. Xi, L.u. Li, J. Dai, Y. Yang, X. Gao, H. Dong, B.o. Jiao, I. Spanopoulos, C.D. Malliakas, X. Hou, M.G. Kanatzidis, Z. Wu, Conjugated organic cations enable efficient self-healing FASnI<sub>3</sub> solar cells, *Joule* 3 (12) (2019) 3072–3087, <https://doi.org/10.1016/j.joule.2019.08.023>.
- [58] M. Li, C. Zhao, Z.-K. Wang, C.-C. Zhang, H.K.H. Lee, A. Pockett, J. Barbé, W.C. Tsoi, Y.-G. Yang, M.J. Carnie, X.-Y. Gao, W.-X. Yang, J.R. Durrant, L.-S. Liao, S.M. Jain, Interface modification by ionic liquid: a promising candidate for indoor light harvesting and stability improvement of planar perovskite solar cells, *Adv. Energy Mater.* 8 (24) (2018) 1801509, <https://doi.org/10.1002/aenm.v8.2410.1002/aenm.201801509>.
- [59] R. Cheng, C.-C. Chung, H. Zhang, F. Liu, W.-T. Wang, Z. Zhou, S. Wang, A. B. Djurišić, S.-P. Feng, Tailoring triple-anion perovskite material for indoor light harvesting with restrained halide segregation and record high efficiency beyond 36%, *Adv. Energy Mater.* 9 (38) (2019) 1901980, <https://doi.org/10.1002/aenm.v9.3810.1002/aenm.201901980>.
- [60] K.-L. Wang, X.-M. Li, Y.-H. Lou, M. Li, Z.-K. Wang, CsPbBr I2 perovskites with low energy loss for high-performance indoor and outdoor photovoltaics, *Sci. Bulletin* 66 (4) (2021) 347–353, <https://doi.org/10.1016/j.scib.2020.09.017>.
- [61] C. Dong, X.-M. Li, C. Ma, W.-F. Yang, J.-J. Cao, F. Igbari, Z.-K. Wang, L.-S. Liao, Lycopene-based bionic membrane for stable perovskite photovoltaics, *Adv. Funct. Mater.* 31 (25) (2021) 2011242, <https://doi.org/10.1002/adfm.v31.2510.1002/adfm.202011242>.
- [62] A. Venkateswararao, J.K.W. Ho, S.K. So, S.-W. Liu, K.-T. Wong, Device characteristics and material developments of indoor photovoltaic devices, *Mater. Sci. Eng. R* 139 (2020) 100517, <https://doi.org/10.1016/j.mser.2019.100517>.
- [63] V. Gupta, A.K.K. Kyaw, D.H. Wang, S. Chand, G.C. Bazan, A.J. Heeger, Barium: an efficient cathode layer for bulk-heterojunction solar cells, *Sci. Rep.* 3 (2013) 1–6, <https://doi.org/10.1038/srep01965>.
- [64] M. Li, F. Igbari, Z.-K. Wang, L.-S. Liao, Indoor thin-film photovoltaics: progress and challenges, *Adv. Energy Mater.* 10 (28) (2020) 2000641, <https://doi.org/10.1002/aenm.v10.2810.1002/aenm.202000641>.
- [65] W.-F. Yang, J.-J. Cao, C. Dong, M. Li, Q.-S. Tian, Z.-K. Wang, L.-S. Liao, Suppressed oxidation of tin perovskite by Catechin for eco-friendly indoor photovoltaics, *Appl. Phys. Lett.* 118 (2) (2021) 023501, <https://doi.org/10.1063/5.0032951>.